AIP | The Journal of Chemical Physics

Fourier moment analysis of velocity-map ion images

Mark J. Bass, Mark Brouard, Andrew P. Clark, and Claire Vallance

Citation: The Journal of Chemical Physics **117**, 8723 (2002); doi: 10.1063/1.1514978
View online: http://dx.doi.org/10.1063/1.1514978
View Table of Contents: http://scitation.aip.org/content/aip/journal/jcp/117/19?ver=pdfcov
Published by the AIP Publishing

JOURNAL OF CHEMICAL PHYSICS VOLUME 117, NUMBER 19 15 NOVEMBER 2002

Fourier moment analysis of velocity-map ion images

Mark J. Bass, Mark Brouard,[a] Andrew P. Clark, and Claire Vallance
Department of Chemistry, The Physical and Theoretical Chemistry Laboratory, South Parks Road, Oxford, OX1 3QZ, United Kingdom

(Received 11 April 2002; accepted 27 August 2002)

An alternative to inverse Abel transform and forward convolution methods is presented for extracting dynamical information from velocity-map ion images. Unlike most competing methods, that presented here does not require the probed three-dimensional distribution to possess cylindrical symmetry. The new method involves analysis of the Fourier moments of images measured in different experimental geometries, and allows speed distributions, angular differential cross sections, and angular momentum alignment and orientation to be determined from raw images of the products of photodissociation and photon-initiated bimolecular reactions. The methodology is developed within the semiclassical framework of Dixon's bipolar moment formalism [R. N. Dixon, J. Chem. Phys. **85**, 1866 (1986)], although it is equally applicable to other common formulations of the product scattering distribution. To allow a comparison of the method with the Abel inversion, which requires that the velocity distribution of the probed product has an axis of cylindrical symmetry, the method is applied to newly acquired experimental images of atomic chlorine produced in the photolysis of NOCl. Extraction of product rotational alignment information is illustrated using newly acquired images of rotationally aligned NO formed by NO_2 photolysis. Application of the Fourier moment methodology to studies of bimolecular reactions is also demonstrated, using simulated images for the reaction $H+D_2 \rightarrow HD(v=0,j=0,9)+D$. *© 2002 American Institute of Physics.* [DOI: 10.1063/1.1514978]

I. INTRODUCTION

Velocity-map ion imaging is a powerful experimental technique that allows direct measurement of a two-dimensional (2D) projection of the velocity distribution of a photofragment or reaction product. Although experimental procedures are now emerging which allow a 2D ''slice'' through the three-dimensional (3D) distribution to be obtained directly (see, for example, Refs. 1 and 2), these slicing methods involve an inherent loss of signal which may not be affordable in all circumstances. For this reason, velocity-map ion imaging, in its 2D projection guise, is likely to remain an important experimental technique for some time. In order to take full advantage of the technique, reliable methods are required for reconstructing the 3D scattering distribution and extracting the dynamical quantities of interest from the 2D images. The two main approaches used to date have been the inverse Abel transform and forward convolution methods.

The inverse Abel transform[3,4] is a direct mathematical transform that returns a slice through the 3D velocity distribution for systems containing an axis of cylindrical symmetry. The transform is ideally suited to studies of simple photolysis systems with no product angular momentum alignment, and has been widely used in the analysis of images from such systems.[5] Recently, Rakitzis[6] has shown that with careful choice of experimental geometries it is also possible to determine the photofragment alignment from a series of Abel-invertible images. Even so, the inversion does have several limitations. A considerable number of researchers are now using imaging techniques to investigate systems for which the symmetry constraints of the inverse Abel transform render it invalid, and alternatives must be found. The transform is also highly sensitive to shot noise in the image. This has become more of a problem with the advent of event-counting techniques,[7] which provide a significant increase in velocity resolution at the expense of a ''grainy'' appearance to the images. For the same reason, systems with inherently low signal levels also present problems for the inverse Abel transform.

An alternative approach involves forward convolution of the image, whereby images are simulated based on a trial scattering distribution and compared with the experimental data. The trial distribution may then be adjusted iteratively until satisfactory agreement is obtained. In a variation on the forward convolution approach, a set of ''basis images'' is simulated and fitted to the experimental images to extract the parameters of interest. One clever example of an iterative approach to generating the 3D scattering distribution, developed by Vrakking,[8] exploits the similarities that exist for cylindrically symmetric systems between the form of the angular and radial distributions of the 3D distribution and of its 2D projection. While, like the Abel inversion, the method is limited to distributions with an axis of symmetry, the returned 3D distributions are virtually noise-free. In general, forward convolution approaches are not limited to cylindrically symmetric distributions, and may be used to analyze images both from imaging experiments using the conventional single molecular beam and from crossed beam experiments. Examples include applications as diverse as photo-

---

[a] Author to whom correspondence should be addressed. Electronic mail: mark.brouard@chemistry.ox.ac.uk

electron imaging,[9] crossed beam studies of inelastic scattering,[10–12] and determination of orbital alignment of atomic photolysis products.[13,14]

Nestorov *et al.* were the first to apply Dixon's semiclassical bipolar moment formalism[15] to the analysis of velocity-map images.[16] Their approach involves forward convolution of basis image functions, which are then fitted to experimental images in order to extract the bipolar moments that characterize vector correlations between the transition dipole moment of the parent molecule and the recoil velocity and angular momentum distribution of the photofragment.

In the current work, a Fourier moment analysis for velocity-map images is presented. The analysis is carried out within the framework of the bipolar moment formalism, though it is equally applicable to density matrix or other representations of the product scattering. In a similar approach to that used in Doppler-resolved laser-induced fluorescence dynamics studies,[17] functions depending on individual terms in the bipolar harmonic expansion of the scattering distribution may be projected out from the images and analyzed separately to obtain information on angular correlations in both photodissociation and photon-initiated bimolecular reactions. The Fourier moment method has several major advantages over previous methods. Unlike the Abel inversion, it does not require the 3D scattering distribution to have an axis of cylindrical symmetry, and may therefore be used to investigate angular momentum alignment and orientation in molecular systems, the presence of which in general destroys the cylindrical symmetry of the detected fragment distribution. Unlike many forward convolution methods, no prior knowledge of the scattering distribution is required. In this sense, the principle advantage of the Abel transform, that it is an ''analytic'' solution to the inversion problem, is retained. Also, the method is relatively insensitive to noise in the image data. This is due to the fact that every angle in the image contributes to each point in the Fourier moments of the image—the functions from which the dynamical parameters of interest are determined. Averaging over the angular coordinate in this way means that the signal-to-noise ratio of the Fourier moments is considerably higher than that of the raw image.

To demonstrate the versatility of the Fourier moment method, we have applied it to newly acquired images of photofragments from two very different photolysis systems. In the first, photolysis of NOCl near 240 nm, we have ignored alignment effects and concentrated on extracting the velocity distribution and velocity-dependent spatial anisotropy distribution of the Cl fragment from the images. The distributions are compared directly with those obtained from an Abel inverted image. One of the principal advantages of the Fourier moment analysis scheme is that it may be applied to images of noncylindrically symmetric distributions. We have demonstrated this using newly acquired images of state-selected NO fragments from 308 nm photolysis of NO_2. The complete set of alignment moments obtained are compared with the results of Doppler resolved laser-induced fluorescence experiments recently carried out in our laboratory. Finally, we also demonstrate the potential use of the analysis scheme in determining differential cross sections from images of reactive scattering products. In a future paper we will apply the method to the determination of electronic orbital alignment in the photodissociation of Cl_2.[18]

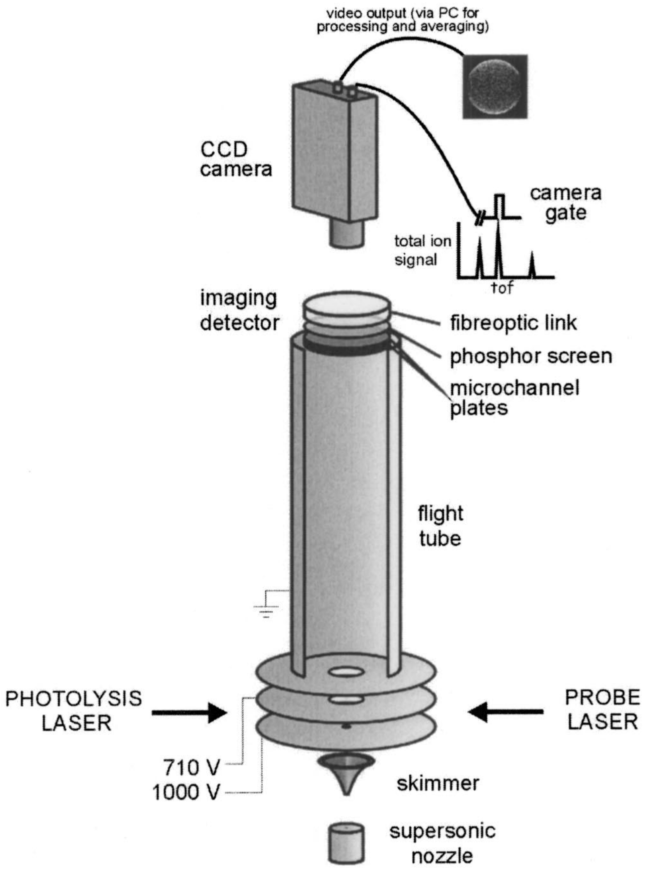

FIG. 1. Schematic of the experimental apparatus.

II. EXPERIMENT

A. NOCl photolysis

NOCl photolysis experiments were carried out using a standard velocity-map ion imaging setup, shown schematically in Fig. 1. A skimmed molecular beam of NOCl seeded in helium passes through a 2 mm hole in the repeller plate and is intersected by a laser beam from a frequency doubled LPD series tunable dye laser, which serves both to photolyze NOCl and to ionize the Cl photofragments *via* $(2+1)$ resonantly enhanced multiphoton ionization (REMPI). Ionized photofragments are extracted along a 40 cm flight tube through 20 mm holes in the extraction plates to a 40 mm chevron microchannel plate detector coupled to a P47 phosphor screen. The resulting images are captured by an intensified charge coupled device camera (Photonic Science) gated to the time-of-flight of the ion of interest, then sent to a PC for signal averaging and processing. Images are generally averaged over 10–20 000 laser shots. Use of velocity-mapping ion optics introduces a calibration factor into the conversion of the radial coordinate of the image into photofragment velocity. This factor was determined as a function of extraction voltage using images of Cl from Cl_2 photolysis and NO from NO_2 photolysis, for which the photofragment velocities may be calculated exactly from known bond dissociation energies.

NOCl was prepared by mixing small amounts of NO_2 and Cl_2 in a helium buffer gas (around 1 part NO_2 to 4 parts Cl_2 up to a partial pressure of $\sim$5% of the total gas pressure). Images were obtained for both ground and spin–orbit excited state Cl photolysis products. Ground state fragments were detected *via* both the $4p\,^4P_{3/2}\leftarrow{}^2P_{3/2}$ and $4p\,^4P_{1/2}\leftarrow{}^2P_{3/2}$ REMPI transitions at 240.46 and 239.84 nm, respectively, and excited state fragments were detected on the $4p\,^4D_{3/2}\leftarrow{}^2P_{1/2}$ transition at 240.17 nm.[19] Images were recorded using both horizontal and vertical laser polarizations.

B. NO_2 photolysis

For the NO_2 photolysis experiments, a beam of 2% NO_2 in helium was intersected by counterpropagating pump and probe laser beams, timed to fire simultaneously. The pump beam was provided by the 308 nm output from a Lambda Physik EMG103 excimer laser. The NO photofragments were probed state selectively by $(1+1')$REMPI, with the resonant photon provided by the doubled dye laser output described previously, and the ionization photon provided by the 308 nm photolysis pulse. Using this scheme it was possible to use an unfocused probe beam, eliminating probe-only signal in which photolysis and one-color $(1+1)$REMPI are effected by the focused dye laser output. NO fragments in $(v=0,N=30)$ were probed on the $(0,0)Q_1(30)$ and $(0,0)R_1(30)$ transitions of the $A(^2\Sigma^+)\leftarrow X(^2\Pi_{1/2})$ band at 224.87 and 224.35 nm, respectively. Images were recorded in two different experimental geometries, denoted HH and HV, denoting the polarizations of the pump and probe lasers as "horizontal" (H) or "vertical" (V) with respect to the plane of the image.

III. THEORY AND ANALYSIS

The basis of the Fourier moment analysis scheme lies in the fact that the intensity distribution in a velocity map image (i.e., the projection of the 3D scattering distribution onto the image plane) may be expressed as a Fourier series in the angular coordinate of the image. Analysis of the Fourier moments of the image, and their dependence on pump–probe geometry and probe transition, then allows information on vector correlations between the electric vector of the photolysis light and product translational and rotational motions to be extracted from the data.

A. Fourier moments of the image

The normalized product scattering distribution following polarized laser photolysis may be expressed as an expansion in bipolar harmonics[15]

$$P(v,\Omega_v,\Omega_j)=\frac{1}{16\pi^2}\sum_{K=0,2}\sum_{k_1,k_2}c(K)[k_1]\times[k_2]b_0^K(k_1,k_2;v)B_0^K(k_1,k_2;\Omega_v,\Omega_j) \qquad (1)$$

with

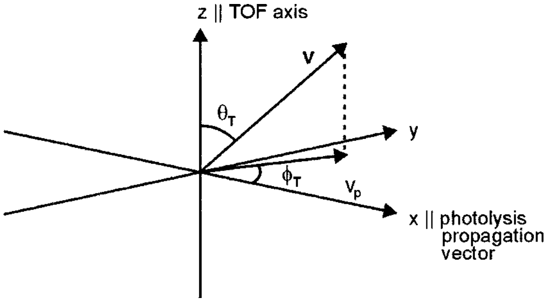

FIG. 2. The time-of-flight frame of reference.

$$B_0^K(k_1,k_2;\Omega_v,\Omega_j)=\sum_q(-1)^K[K]^{1/2}\begin{pmatrix}k_1 & K & k_2\\ q & 0 & -q\end{pmatrix}\times C_{k_1q}(\Theta_v,\Phi_v)C_{k_2-q}(\Theta_j,\Phi_j), \qquad (2)$$

where $[K]=2K+1$, $c(0)=1$, $c(2)=2/5$ for a photolysis process, and $c(2)=\beta/5$ for a photon-initiated reaction.[17] The angles $\Omega_v=(\Theta_v,\Phi_v)$ and $\Omega_j=(\Theta_j,\Phi_j)$ are the polar coordinates of the product velocity and rotational angular momentum vectors, and the (body fixed) bipolar moments $b_0^K(k_1,k_2;v)$ are the (in general) speed-dependent coefficients of the expansion. The angular coordinates Ω_v and Ω_j are defined relative to the *lab frame* axis system, in which z is parallel to the photolysis polarization vector and x lies along the photolysis propagation vector. For clarity in the following discussion, two further reference frames are now defined. In the *time-of-flight frame*, shown in Fig. 2, z lies along the time-of-flight axis and x along the photolysis propagation vector; the polar coordinates of the product velocity vector in this frame are denoted Ω_T. The *detection frame* has z along the probe laser propagation axis and x along the probe polarization vector.

The detection frame defined previously is the customary frame in which to describe the intensity of the velocity-map image arising from ions produced via a REMPI detection scheme.[15,20,21] However, the time-of-flight frame provides the most natural *coordinate system* for describing velocity-map ion images: θ_T is the angle the product velocity vector makes with the time-of-flight axis, while ϕ_T is the polar coordinate of the image, i.e., the angle made between the projection of the product velocity onto the image plane and the x axis. For this reason, it is convenient to express the scattering distribution in time-of-flight-frame coordinates by rewriting the lab-frame bipolar harmonics appearing in Eq. (1) as a linear combination of time-of-flight-frame bipolar harmonics. The expansion coefficients are simply the rotation matrix elements $D^{k_1}_{q'q}(\alpha,\beta,\gamma)$, where (α,β,γ) are the Euler angles describing the rotation

$$B_0^K(k_1,k_2;\Omega_v,\Omega_j)=\sum_q(-1)^K[K]^{1/2}\begin{pmatrix}k_1 & K & k_2\\ q & 0 & -q\end{pmatrix}\times C_{k_2-q}(\Theta_j,\Phi_j)\times\sum_{q'}D^{k_1}_{q'q}(\alpha,\beta,\gamma)C_{k_1q'}(\theta_T,\phi_T). \qquad (3)$$

Substituting Eq. (3) into Eq. (1), the lab-frame product scattering distribution becomes

$$P(v,\Omega_T,\Omega_j)=\frac{1}{16\pi^2}\sum_{K=0,2}\sum_{k_1k_2}c(K)[k_1][k_2]b_0^K(k_1,k_2;v)\times\sum_q(-1)^K[K]^{1/2}\begin{pmatrix}k_1 & K & k_2\\ q & 0 & -q\end{pmatrix}\times C_{k_2-q}(\Theta_j,\Phi_j)\sum_{q'}D^{k_1}_{q'q}(\alpha,\beta,\gamma)\times C_{k_1q'}(\theta_T,\phi_T). \tag{4}$$

The lab-frame expression for the projection of the scattering distribution onto the image plane, $P_{xy}(v_p,\phi_T,\Omega_j)$, is obtained by integrating Eq. (4) over the time-of-flight axis using the Jacobian, $dv_{\mathrm{TOF}}/dv=[v^2/(v^2-v_p^2)]^{1/2}$, where v_p is the velocity projection onto the image plane

$$P_{xy}(v_p,\phi_T,\Omega_j)=\frac{1}{16\pi^2}\sum_{K=0,2}\sum_{k_1k_2}c(K)[k_1][k_2]\times\int_{v_p}^{\infty}b_0^K(k_1,k_2;v)\sum_q(-1)^K[K]^{1/2}\times\begin{pmatrix}k_1 & K & k_2\\ q & 0 & -q\end{pmatrix}C_{k_2-q}(\Theta_j,\Phi_j)\times\sum_{q'}D^{k_1}_{q'q}(\alpha,\beta,\gamma)[C_{k_1q'}(\theta_T,\phi_T)+C_{k_1q'}(\pi-\theta_T,\phi_T)]\left(\frac{v^2}{v^2-v_p^2}\right)^{1/2}v_p\,dv. \tag{5}$$

Using the fact that $C_{k_1q'}(\pi-\theta_T,\phi_T)=(-1)^{k_1+q'}C_{k_1q'}(\theta_T,\phi_T)$, the rotational moments of the projected distribution are then given by

$$\rho_q^k(v_p,\phi_T)_{\mathrm{lab}}=\int C_{kq}(\Theta_j,\Phi_j)P_{xy}(v_p,\phi_T,\Omega_j)d\Omega_j=\frac{1}{4\pi}\sum_{K=0,2}c'(K)\sum_{k_1}[k_1]\begin{pmatrix}k_1 & K & k\\ q & 0 & -q\end{pmatrix}\times\sum_{q'}D^{k_1}_{q'-q}(\alpha,\beta,\gamma)[1+(-1)^{k_1+q'}]\times e^{iq'\phi_T}\int_{v_p}^{\infty}b_0^K(k_1,k;v)C_{k_1q'}(\theta_T,0)\times\left(\frac{v^2}{v^2-v_p^2}\right)^{1/2}v_p\,dv, \tag{6}$$

where $c'(K)=(-1)^K[K]^{1/2}c(K)$.

TABLE I. Euler angles for the lab to time-of-flight (α, β, γ) and lab to detection frame (α',β',γ') transformations for some commonly used experimental geometries. The notation HH, HV, etc., denotes the polarizations of the pump and probe lasers (horizontal or vertical) relative to the image plane.

Pump–probe propagation	Pump–probe polarization	(α, β, γ)	(α',β',γ')
Copropagating	HH	($\pi/2$, $\pi/2$, $-\pi/2$)	(π, $-\pi/2$, 0)
Copropagating	VV	(0, 0, 0)	(π, $\pi/2$, 0)
Counterpropagating	HH	($\pi/2$, $\pi/2$, $-\pi/2$)	(0, $-\pi/2$, 0)
Counterpropagating	HV	($\pi/2$, $\pi/2$, $-\pi/2$)	(0, $-\pi/2$, $\pi/2$)
Counterpropagating	VH	(0, 0, 0)	(0, $-\pi/2$, $-\pi/2$)
Counterpropagating	VV	(0, 0, 0)	(0, $-\pi/2$, 0)

The detection-frame moments are obtained by rotating Eq. (6) into the detection frame (Euler angles α', β', γ'),

$$\rho^k_{q''}(v_p,\phi_T)_{\mathrm{det}}=\frac{1}{4\pi}\sum_{K=0,2}c'(K)\sum_{k_1}[k_1]\times\sum_q\begin{pmatrix}k_1 & K & k\\ q & 0 & -q\end{pmatrix}D^k_{qq''}(\alpha',\beta',\gamma')\times\sum_{q'}D^{k_1}_{q'-q}(\alpha,\beta,\gamma)[1+(-1)^{k_1+q'}]\times e^{iq'\phi_T}\int_{v_p}^{\infty}b_0^K(k_1,k;v)C_{k_1q'}(\theta_T,0)\times\left(\frac{v^2}{v^2-v_p^2}\right)^{1/2}v_p\,dv. \tag{7}$$

The resulting expression may be written more compactly as

$$\rho^k_{q''}(v_p,\phi_T)_{\mathrm{det}}=\frac{1}{4\pi}\sum_{q'}e^{iq'\phi_T}\sum_{K=0,2}\sum_{k_1}[1+(-1)^{k_1+q'}]\times f_0^K(k_1,k,q',q'',R,R')F_0^K(k_1,k,q';v_p), \tag{8}$$

where

$$f_0^K(k_1,k,q',q'',R,R')=c'(K)[k_1]\sum_q\begin{pmatrix}k_1 & K & k\\ q & 0 & -q\end{pmatrix}D^k_{qq''}(R')D^{k_1}_{q'-q}(R) \tag{9}$$

and

$$F_0^K(k_1,k,q';v_p)=\int_{v_p}^{\infty}b_0^K(k_1,k;v)C_{k_1q'}(\theta_T,0)\times\left(\frac{v^2}{v^2-v_p^2}\right)^{1/2}v_p\,dv \tag{10}$$

and R and R' are the Euler angles for the rotations from the time-of-flight frame to the lab frame, and from the lab frame to the detection frame, respectively. The specific Euler angles for typically used copropagating and counterpropagating pump–probe geometries are given in Table I. While the derivation of the above-given expression is somewhat complex, the final result is fairly simple. Equation (8) represents a Fourier expansion in the angle ϕ_T, with the Fourier coefficients given by sums of products of the factors $f_0^K(\cdots)$ and

$F_0^K(\cdots)$. The $f_0^K(\cdots)$ parameters depend only on experimental geometry and are straightforward to calculate, while the $F_0^K(\cdots)$ factors characterize the dynamics. Each of the $F_0^K(\cdots)$ factors depends on a single bipolar moment $b_0^K(k_1,k;v)$. Note that the bipolar moments in Eq. (10) have not been renormalized to the more commonly employed $\beta_0^K(k_1,k;v)$ moments. The appropriate normalization constants may be found in Ref. 15.

The Hertel–Stoll scheme[22] may be used to transform the rotational moments $\rho_{q''}^k$ of Eq. (8), which in general have both real and imaginary parts, into the real quantities $\rho_{q''+}^k$ and $\rho_{q''-}^k$ (the subscript specifying the detection frame will now be dropped for ease of notation):

$$\rho_{q''+}^k=(-1)^{q''}(2-\delta_{q''0})^{1/2}\,\mathrm{Re}[\rho_{q''}^k],\quad q''\geqslant 0,$$
$$\rho_{q''-}^k=(-1)^{q''}2^{1/2}\,\mathrm{Im}[\rho_{q''}^k],\quad q''>0. \tag{11}$$

In general, for planar symmetric distributions, such as that resulting from photodissociation of a nonchiral molecule, only the terms $\rho_{q''+}^k$ with even *k*, and $\rho_{q''-}^k$ with odd *k*, are nonzero. Furthermore, for the present application, which employs linearly polarized pump *and* probe light, only the $\rho_{q''+}^k$ moments with even q'' are nonzero. The rotational moments of Eq. (8) then become

$$\begin{aligned}\rho_{q''+}^k(v_p,\phi_T)=\frac{(-1)^{q''}(2-\delta_{q''0})^{1/2}}{4\pi}\sum_{K=0,2}\sum_{k_1}\Big\{&[1+(-1)^{k_1}]f_0^K(k_1,k,0,q'';R,R')\times F_0^K(k_1,k,0;v_p)\\&+\sum_{q'>0}\cos(q'\phi_T)[1+(-1)^{k_1+q'}][f_0^K(k_1,k,q',q'';R,R')+(-1)^{q'}f_0^K(k_1,k,-q',q'';R,R')]\\&\times F_0^K(k_1,k,q';v_p)\Big\},\quad q''\geqslant 0.\end{aligned} \tag{12}$$

Equations (8)–(12) are equivalent to those published previously by Nestorov *et al.*[16]

B. Image analysis

1. Fourier analysis

In systems for which there is no product angular momentum alignment, only the ρ_0^0 rotational moment is nonzero, simplifying the analysis considerably. There are three nonzero $F_0^K(\cdots)$ functions, which may be extracted from two images obtained using different experimental geometries. Since in the one-laser experiments carried out on NOCl photolysis the only two geometries available were copropagating pump and probe with the laser polarization vector either horizontal or vertical with respect to the image plane, the analysis was limited to obtaining the bipolar moments of the ρ_0^0 rotational moment. Higher moments were assumed to be zero, an approximation that was justified by the insensitivity of the images to the probe transition. For the two geometries used in the one-color NOCl experiments, after substitution for the geometrical factors $f_0^K(\cdots)$, Eq. (12) becomes

$$\begin{aligned}\rho_0^0(v_p,\phi_T)_H&=F_0^0(0,0,0,v_p)-F_0^2(2,0,0,v_p)\\&\quad-\sqrt{6}F_0^2(2,0,2,v_p)\cos 2\phi_T,\\\rho_0^0(v_p,\phi_T)_V&=F_0^0(0,0,0,v_p)+2F_0^2(2,0,0,v_p),\end{aligned} \tag{13}$$

in which the subscripts *H* and *V* denote the laser polarization with respect to the image plane.

The Fourier moments $c_n(v_p)$ are extracted from the experimental data by carrying out a series of integrals over the angular coordinate ϕ_T of the image $\mathcal{I}(v_p,\phi_T)\equiv\mathcal{I}(v_x,v_y)v_p$,

$$c_n(v_p)=N\int_0^{2\pi}\mathcal{I}(v_x,v_y)\cos(n\phi_T)v_p\,d\phi_T, \tag{14}$$

where the normalization constant *N* is equal to 1 when $n=0$ and 2 when $n>0$. In obtaining these normalization constants the Fourier series has been defined as

$$\begin{aligned}\mathcal{I}(v_p,\phi_T)=c_0(v_p)+2\Big\{&\sum_{n>0}c_n(v_p)\cos n\phi_T\\&+\sum_{n>0}c_n'(v_p)\sin n\phi_T\Big\}.\end{aligned} \tag{15}$$

With linearly polarized pump and probe radiation, *n* is restricted to even terms [as seen from Eq. (12)], and the c_n' coefficients are all zero. The even c_n' moments only differ from zero for the $\rho_{q''-}^k$ moments with *k* odd, and could be probed with circularly polarized probe radiation. From Eq. (13) it is seen that for the horizontal geometry the zeroth and second Fourier moments are nonzero, while for the vertical geometry only the zeroth moment is nonzero, i.e.,

$$\begin{aligned}c_0(v_p)_H&=F_0^0(0,0,0,v_p)-F_0^2(2,0,0,v_p),\\c_2(v_p)_H&=-\sqrt{6}F_0^2(2,0,2,v_p),\\c_0(v_p)_V&=F_0^0(0,0,0,v_p)+2F_0^2(2,0,0,v_p).\end{aligned} \tag{16}$$

TABLE II. Expressions for *nonzero* Fourier moments of experimentally accessible $\rho^k_{q''+}(v_p,\phi_T)$ rotational moments for velocity-map images of NO photofragments from NO_2 photolysis, obtained using $(1+1')$REMPI.

Geometry	Moment	Fourier moments
HH	ρ_0^0	$c_0(v_p)=F_0^0(0,0,0;v_p)-F_0^2(2,0,0;v_p)$ $c_2(v_p)=-2.449F_0^2(2,0,2;v_p)$
	$\rho_0^2-3\rho_{2+}^2$	$c_0(v_p)=4.691F_0^0(2,2,0;v_p)-1.240F_0^2(0,2,0;v_p)$ $-1.069F_0^2(2,2,0;v_p)-2.676F_0^2(4,2,0;v_p)$ $c_2(v_p)=7.482F_0^0(2,2,2;v_p)-4.536F_0^2(2,2,2;v_p)$ $-5.270F_0^2(4,2,2;v_p)$ $c_4(v_p)=-5.498F_0^2(4,2,4;v_p)$
HV	ρ_0^0	$c_0(v_p)=F_0^0(0,0,0;v_p)-F_0^2(2,0,0;v_p)$ $c_2(v_p)=-2.449F_0^2(2,0,2;v_p)$
	$\rho_0^2-3\rho_{2+}^2$	$c_0(v_p)=-5.928F_0^0(2,2,0;v_p)+0.839F_0^2(0,2,0;v_p)$ $-1.069F_0^2(2,2,0;v_p)+3.157F_0^2(4,2,0;v_p)$ $c_2(v_p)=-2.005F_0^0(2,2,2;v_p)+4.536F_0^2(2,2,2;v_p)$ $+5.270F_0^2(4,2,2;v_p)$ $c_4(v_p)=1.473F_0^2(4,2,4;v_p)$

For this system, in which there is no alignment, it is a simple matter to solve these equations to obtain expressions for the $F_0^K(\cdots)$ functions:

$$\begin{aligned}
F_0^0(0,0,0,v_p)&=\tfrac{1}{3}[c_0(v_p)_V+2c_0(v_p)_H],\\
F_0^2(2,0,0,v_p)&=\tfrac{1}{3}[c_0(v_p)_V-c_0(v_p)_H], \qquad (17)\\
F_0^2(2,0,2,v_p)&=-\frac{1}{\sqrt{6}}c_2(v_p)_H.
\end{aligned}$$

These functions are then fitted to a basis set, as described in more detail later, to return the bipolar moments $b_0^K(k_1,k;v)$, which contain all the required dynamical information.

In systems with alignment, ρ_0^0 and higher rotational moments may be projected out by taking the appropriate linear combinations of the Fourier moments of images measured on different REMPI transitions using the intensity expressions developed by Greene and Zare[23] and Kummel, Sitz, and Zare.[20,21] In terms of the detection frame moments $\rho^k_{q''\pm}$, the raw image may be written

$$\mathcal{I}(v_p,\phi_T)=C\sum_{k,q\geqslant 0}P^k_{q''\pm}(i,f)\rho^k_{q''\pm}(v_p,\phi_T), \qquad (18)$$

where $P^k_{q''\pm}(i,f)$ is a moment of the line strength for a transition between states i and f and depends on the REMPI scheme [e.g., the line strength moments for $(1+1)$REMPI will differ from those for a $(2+1)$ process], and C is a constant, dependent (among other factors) on the populations in initial state i. The values taken by the indices k and q'' depend on the number of photons and their polarization.

For a $(1+1')$REMPI detection scheme, as used in the NO_2 experiments, if we assume the ionization step is saturated, the intensity of the image is equivalent to that provided by Dixon in his description of a chemiluminescence experiment,[15]

$$\begin{aligned}
\mathcal{I}(v_p,\phi_T)=\tfrac{1}{3}I_0[\rho_0^0(v_p,\phi_T)-\tfrac{1}{2}h^{(2)}(J_i,J_f)\\
\times\{\rho_0^2(v_p,\phi_T)-3\rho_{2+}^2(v_p,\phi_T)\}], \qquad (19)
\end{aligned}$$

where $h^{(2)}(J_i,J_f)$ is a line strength factor depending on the initial and final states of the resonant transition, taking the value $+1$ for a Q branch transition, $-J_i/(2J_i+3)$ for a P branch transition, and $-(J_i+1)/(2J_i-1)$ for an R branch transition. Both of the transitions used to detect NO photofragments in the present work have an intensity contribution from overlapping satellite lines. The correct $h^{(2)}(J_i,J_f)$ factors in this case are therefore an average over the values for the two overlapping lines, weighted by the transition probability for each line.

Before proceeding with the analysis, the image moments must be properly normalized to take account of the total rotational alignment. The appropriate normalization constants are determined by integrating Eq. (19) over the angular coordinate of the image,

$$\begin{aligned}
I\propto 1-\tfrac{1}{2}h^{(2)}(J_i,J_f)[2\,f_0^2(0,2,0,0)\\
-6\sqrt{2}f_0^2(0,2,0,2)]b_0^2(0,2). \qquad (20)
\end{aligned}$$

The value of the $b_0^2(0,2)$ bipolar moment has been measured independently[33] to be -0.23 ± 0.02. Once the image moments have been normalized, Eq. (19) may be used to project out $\rho_0^0(v_p,\phi_T)$ and the combination $\rho_0^2(v_p,\phi_T)-3\rho_{2+}^2(v_p,\phi_T)$ by taking linear combinations of experimentally determined Fourier moments for different rotational branches involving the same lower state. For the Q and R line transitions used in the present work, the appropriate linear combinations are

$$\begin{aligned}
\rho_0^0(v_p,\phi_T)&=\frac{h_R^{(2)}\mathcal{I}_Q-h_Q^{(2)}\mathcal{I}_R}{h_R^{(2)}-h_Q^{(2)}},\\
\rho_0^2(v_p,\phi_T)-3\rho_{2+}^2(v_p,\phi_T)&=\frac{2(\mathcal{I}_Q-\mathcal{I}_R)}{h_R^{(2)}-h_Q^{(2)}}.
\end{aligned} \qquad (21)$$

Expressions for the Fourier moments of these images [analogous to those presented for NOCl photolysis in Eq. (13)] are given in Table II.

In the case of aligned systems, rather than extracting individual $F_0^K(\cdots)$ functions from the data, it is often simpler to fit the basis functions directly to the Fourier moments of the population and alignment-dependent images of Eq. (21) in order to extract the bipolar moments. In the present case, the expressions appearing in Table II have been used to fit the experimentally determined Fourier moments. Whether fitting the $F_0^K(\cdots)$ functions or fitting the Fourier moments directly, the basis functions used to fit the data consist of a set of simulated $F_0^K(\cdots)$ functions. There are two cases to consider.

i. Single recoil velocity. In systems for which the detected product has a single, well-defined velocity (common in photolysis of diatomics or photolysis of triatomics in which the diatomic fragment is probed state-selectively, as in the present experiments on the photolysis of NO_2) the fitting procedure becomes very simple. Equation (10) reduces to

$$\begin{aligned}F_0^K(k_1,k,q';v_p)&=\int_0^\infty b_0^K(k_1,k;v)\,\delta(v-v_0)\,C_{k_1q'}(\theta_T,0)\\&\quad\times\left(\frac{v^2}{v^2-v_p^2}\right)^{1/2}v_p\,dv\\&=b_0^K(k_1,k)\,C_{k_1q'}(\theta_T,0)\left(\frac{v_0^2}{v_0^2-v_p^2}\right)^{1/2}v_p\,.\end{aligned}\tag{22}$$

The basis functions are then simply the analytical functions $C_{k_1q'}(\theta_T,0)\ [v_0^2/(v_0^2-v_p^2)]^{1/2}v_p$ and the fitting parameters are the bipolar moments $b_0^K(k_1,k)$. Note that the angle θ_T appearing in the spherical harmonics is calculated using the equivalence $\theta_T=\sin^{-1}(v_p/v)$ (see Fig. 2). If fitting to experimentally determined $F_0^K(\cdots)$ functions, the bipolar moments are simply the scaling factors between these functions and the (properly normalized) experimental data. If fitting the Fourier moments, the basis functions are used in conjunction with the mathematical expressions for the image Fourier moments [e.g., those in Table II for $(1+1')$REMPI] and best fit values for the bipolar moments determined from a numerical fitting routine.

ii. Multiple recoil velocities. In systems for which the probed product has a distribution of velocities, as is the case for the Cl photofragments in the UV photolysis of NOCl, the bipolar moments are velocity dependent. Each moment may be expressed as an expression in Legendre polynomials (or any other suitable set of functions)

$$b_0^K(k_1,k;v')=\tfrac{1}{2}\sum_n\ (2n+1)\,a_n P_n(v')\tag{23}$$

and the corresponding $F_0^K(\cdots)$ function is fitted to a set of basis functions

$$\begin{aligned}F_0^K(k_1,k,q';v_p)_n&=\frac{1}{2}\int_{v_p}^\infty(2n+1)P_n(v')\,C_{k_1q'}(\theta_T,0)\\&\quad\times\left(\frac{v^2}{v^2-v_p^2}\right)^{1/2}v_p\,dv\end{aligned}$$

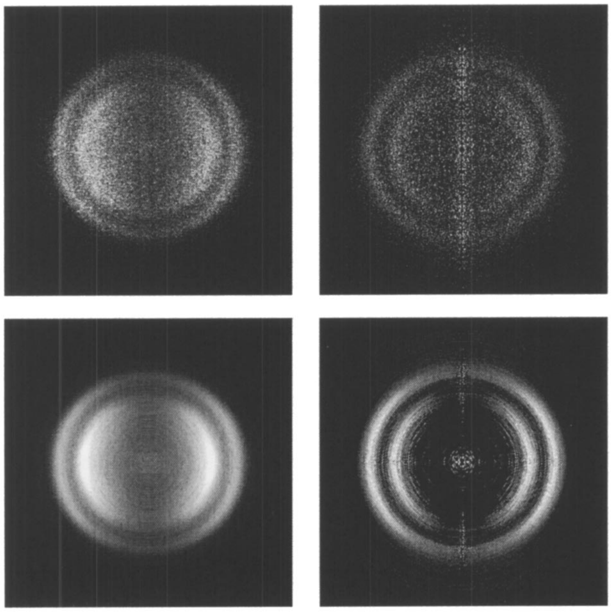

FIG. 3. Fourier smoothing: Raw image (top left); inverse Abel transform of raw image (top right); Fourier smoothed image (bottom left); and inverse Abel transform of smoothed image (bottom right).

in order to determine the expansion coefficients a_n. In the above-given expressions, $v'=2(v/v_{\max})-1$ is a reduced velocity parameter lying between -1 and 1, the limits between which the Legendre polynomials form an orthogonal basis. In the present work, a genetic algorithm fitting program was used to carry out the analysis.

2. Inverse Abel transform analysis

In the next section, the results of the Fourier moment analysis on images of NOCl photolysis fragments are compared with product scattering distributions determined using the inverse Abel transform. As mentioned previously, one of the problems with the inverse Abel transform is that it is highly sensitive to experimental noise. The transform works best on smooth functions, and does not cope well with the ‘‘graininess’’ intrinsic to event-counted velocity map images. A common method for overcoming this problem is to carry out a three-point Gaussian blur on the images before calculating their inverse Abel transform. This overcomes the noise problem to some extent, but also leads to a small loss in velocity resolution. In the present work, a procedure has been developed for smoothing the images which does not entail any loss in resolution. By taking advantage of the fact that a velocity map image may always be expressed as a Fourier expansion in the angular coordinate of the image, the Fourier moments of the image may be extracted using Eq. (14) and used to reconstruct the image using Eq. (15). An example of this ‘‘Fourier smoothing’’ and its effect on the inverse Abel transform is shown in Fig. 3. There is a marked improvement in the inverted image following the smoothing procedure, with a significant reduction in centerline noise. The reduction of graininess in the Fourier-smoothed image relative to the raw image is also reflected in the Abel inversions of the two images. Similar results have been achieved by Vrakking,[8] although we believe the present method might

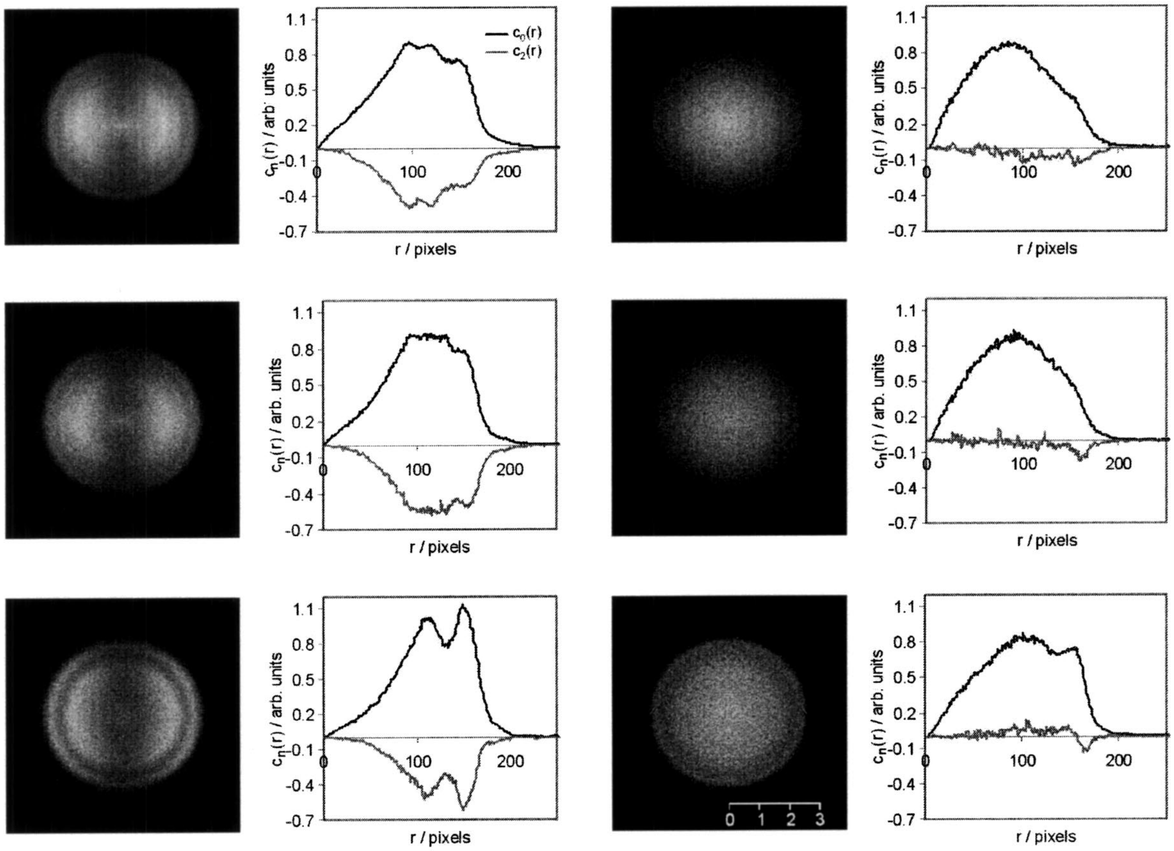

FIG. 4. Cl photofragment images following NOCl photolysis together with their zeroth- and second-order Fourier moments. The left-hand column shows images and moments measured with horizontal laser polarization and the right-hand column with vertical polarization relative to the image plane. From top to bottom, the images are: Cl($^2P_{3/2}$) detected *via* the $4p\ ^4P_{1/2}$ state; Cl($^2P_{3/2}$) detected *via* the $4p\ ^4P_{3/2}$ state; and Cl($^2P_{1/2}$) detected *via* the $4p\ ^4D_{3/2}$ state. The scale on the lower right-hand image denotes the velocity in km s^{-1}.

be simpler to implement. It should be emphasized at this point that, unlike the Fourier moment fitting method described previously, the Abel inversion (and the inversion method of Vrakking[8]) may only be used for images of a distribution containing an axis of cylindrical symmetry.

IV. RESULTS AND DISCUSSION

A. NOCl photolysis

Velocity map images of the Cl($^2P_{3/2}$) and Cl($^2P_{1/2}$) products of NOCl photolysis near 240 nm are shown in Fig. 4 for the two experimental geometries used. Also shown are the zeroth- and second-order Fourier moments of the images. Figure 5 shows the $F_0^K(\cdots)$ functions extracted from the Fourier moments and the fits to these functions using the basis set method described previously. The bipolar moments returned from the analysis are also shown, and compared with those returned from an inverse Abel transform analysis. Note that the $b_0^0(0,0;v)$ moment is simply the fragment speed distribution, while the velocity-dependent spatial anisotropy parameter is given by $\beta(v)=2b_0^2(2,0;v)/b_0^0(0,0;v)$. In Fig. 6, the product translational energy distributions are plotted.

The product distributions extracted from the images using the two different analyses are in good agreement with one another. The velocity resolution of the Fourier moment analysis is dependent on the number of basis functions used in the Legendre polynomial expansion of the bipolar moments. Using ten basis functions the general shape of the distribution is reproduced, and as the number of basis functions is increased, the finer details of the distribution emerge. In the fits presented in Fig. 5, around 50 basis functions were used, allowing most of the features present in the alternative inverse Abel transform analysis to be reproduced. The fitting parameters for the $F_0^2(2,0,0;v_p)$ and $F_0^2(2,0,2;v_p)$ functions were constrained to be the same, since these two functions depend on the same bipolar moment $b_0^2(2,0;v)$.

NOCl photolysis has been studied previously at a number of wavelengths in the range from 193 to 248 nm.[24–29] In this region, photolysis occurs *via* the *A* band, which is though to consist of three partially overlapping electronic transitions.[25] The photodissociation dynamics are strongly dependent on photolysis wavelength, and a wide range of β parameters and photofragment velocity distributions have been reported. These have been summarized previously by Felder and Morley[25] and by Matsumi and co-workers.[26] Measured photofragment velocity distributions are generally strongly bimodal,[24–26] with similar anisotropy for the two velocity components, though some studies have indicated a slightly lower anisotropy for the faster component, particularly at shorter wavelengths. Previously measured β parameters range from 0.45 for the fast component for photolysis at 193 nm[24] to 1.8 near 235 nm.[26] Measurements at 248 nm

a) Cl probed via $4p^4P_{3/2}$

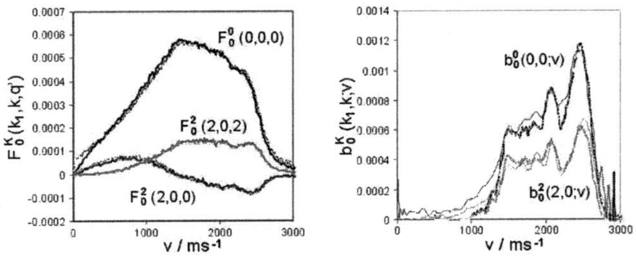

b) Cl probed via $4p^4P_{1/2}$

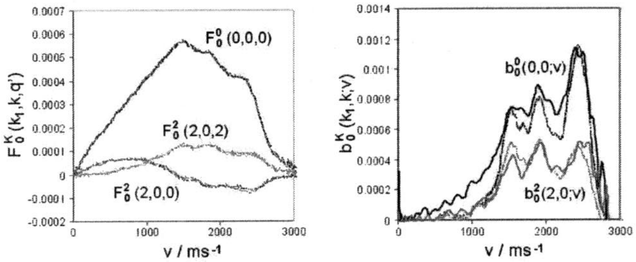

c) Cl* probed via $4p^4D_{3/2}$

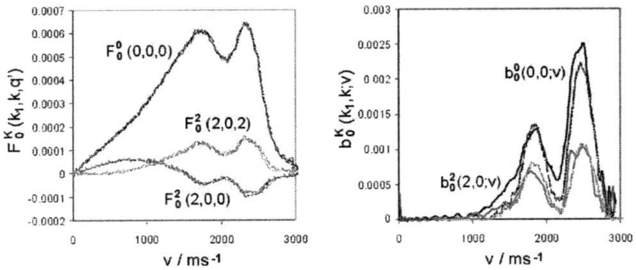

FIG. 5. $F_0^K(\cdots)$ functions extracted from the experimental data (solid lines) and fits to these functions using the basis set expansion method detailed in the text (dotted lines). Also shown are the $b_0^0(0,0;v)$ and $b_0^2(2,0;v)$ bipolar moments returned from the fit (solid lines), together with those obtained from the images using the inverse Abel transform (dotted lines).

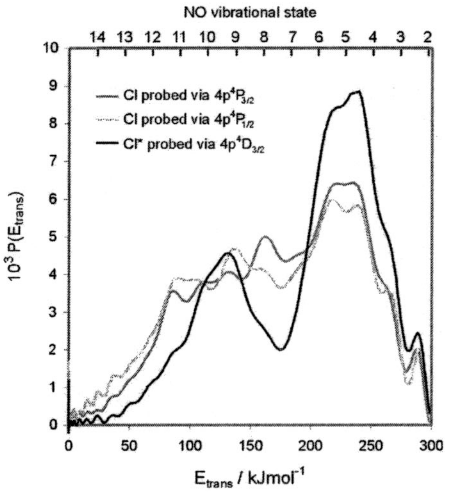

FIG. 6. Translational energy distributions for the products of NOCl photolysis. The corresponding vibrational energy levels of the NO photofragment are marked along the top axis.

give a β value of around 1.2.[25] Apart from the work of Matsumi and co-workers, these measurements were carried out using techniques such as photofragment translational spectroscopy, in which it was not possible to resolve the two spin–orbit states of the Cl photofragment. The resulting distributions therefore represent an average over the two spin–orbit states. Matsumi and co-workers used photofragment ion imaging (as opposed to the higher resolution velocity map ion imaging used in the present study) to detect the Cl products state selectively, and observed significant differences between the velocity distributions of the ground and excited state fragments.[26] He concluded that the observed product distributions were consistent with initial excitation to a common upper electronic state (labeled A_b), followed by a sequence of strong nonadiabatic interactions as the photofragments separate, both at small internuclear separation (due to an avoided crossing) and at large internuclear distances. Two other excited states, labeled A_c and A_a, were cited as being important at short and long wavelengths, respectively. It was suggested that the lower β parameter and fragment internal energy noted in the 248 nm experiments[25] were due to transitions to the A_a electronic state, probably in conjunction with a contribution from the A_b state.

In the present work, the speed distributions for Cl formed in the $^2P_{3/2}$ and $^2P_{1/2}$ states are markedly different (see Fig. 5). Both display a large peak near 2500 $\mathrm{m\,s^{-1}}$, corresponding to formation of the NO cofragment in $v=5$. However, the speed distribution of spin–orbit excited Cl is clearly bimodal, peaking again at 1870 $\mathrm{m\,s^{-1}}$ (corresponding to NO formation in $v=9$ or 10) while that of the ground state photofragment is much broader, with two lower energy peaks in the distribution corresponding to NO formation in $v=9$ and $v=11$. The anisotropy is fairly independent of velocity. The two sets of images collected for the ground state photofragment on the $4p\,^4P_{3/2}\leftarrow{}^2P_{3/2}$ and $4p\,^4P_{1/2}\leftarrow{}^2P_{3/2}$ transitions yield velocity-averaged β parameters of 1.09 and 0.94 (while the discrepancy in values is probably within experimental error, small variations may arise from the fact that since these are single laser experiments, the photolysis energy is slightly different for the two detection schemes, at 5.157 and 5.171 eV, respectively). β for the excited state is 0.90 at a photolysis energy of 5.164 eV. These values are somewhat lower than those measured by Matsumi and co-workers at a slightly shorter wavelengths, a discrepancy that may be due in part to involvement of the A_a state, but is also likely to reflect the higher rotational temperature of the molecular beam in the current experiments. Rotation of the parent NOCl molecule during dissociation reduces the vector correlation between the parent transition dipole moment and the fragment velocity, leading to a reduced value of β. Attempts to treat the effects of molecular rotation quantitatively have been made by several researchers.[30–32]

Though quantitative measurements on the spin–orbit ratio of the products were not carried out, signal levels would indicate that Cl is formed predominantly in the $^2P_{1/2}$ excited spin–orbit state following 240 nm photolysis. This is consistent with previous measurements at 248 nm[25] and implies that the dissociation dynamics are somewhat different from those at 235 nm, for which branching ratios Cl*:Cl have been reported as 0.3[26] and 0.31±0.02.[27] Comparison of the

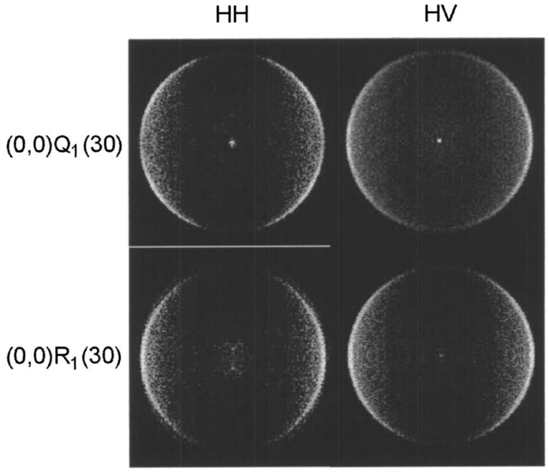

FIG. 7. Photofragment images for the NO($v=0,N=30$) products of 308 nm NO_2 photolysis. Products were detected on the $(0,0)Q_1(30)$ and $(0,0)R_1(30)$ transitions in HH and HV counterpropagating geometries. For the $(0,0)Q_1(30)$ transition in the HH geometry the contribution of a fourth-order Fourier moment c_4 to the image, which can only arise because of photofragment rotational alignment, is clearly visible.

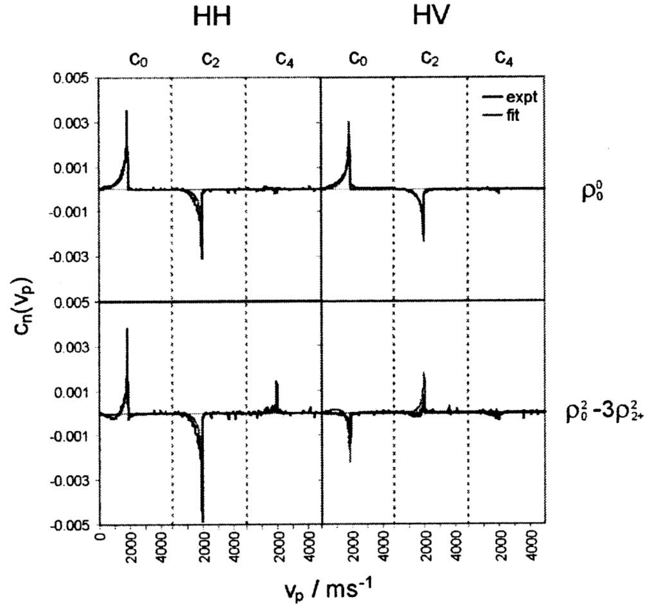

FIG. 8. Experimentally determined Fourier moments of the ρ_0^0 and $\rho_0^2-3\rho_{2+}^2$ rotational moments of the NO product scattering distribution following 308 nm photolysis of NO_2. Fits to the data using the methodology detailed in the text are also shown.

translational energy distributions measured in the present work with the data available in the literature reveals a systematic increase in the importance of the fast component of the bimodal distribution relative to the slow component as the wavelength increases. If the different peaks in the measured velocity distributions were associated with dissociation on different potential energy surfaces, as suggested by Matsumi and co-workers[26] and Felder *et al.*,[24,25] the data would imply involvement of at least two surfaces. The lower energy surface is associated with higher translational energy release and hence lower NO vibrational excitation.

B. NO_2 photolysis

Velocity map images of the NO photofragments for the HH and HV geometries and $Q_1(30)$ and $R_1(30)$ transitions are shown in Fig. 7. Fourier moments and fits to the data for the ρ_0^0 and $\rho_0^2-3\rho_{2+}^2$ rotational moments (discussed in Sec. III B 1) are shown in Fig. 8. The bipolar moments obtained from the fitting procedure are given in Table III, together with data from the only previous set of measurements at 308 nm, carried out by Brouard *et al.*[33] for NO in $N=29$ using Doppler-resolved laser-induced fluorescence (LIF) using the $P_1(29)$ transition. The results of the current measurements, which assume that the two lambda doublet components are identically polarized, are in excellent agreement with those of the earlier experiments, and reinforces the reliability of both the ion images and the data analysis procedures.

The fact that the bipolar moments are consistently of somewhat greater magnitude than the previous study is accounted for by the lower rotational temperature of the parent molecule; the Doppler-resolved LIF experiments were carried out at room temperature in a bulb, while the imaging experiments utilize a molecular beam. The limiting value of β, based on the orientation of the transition dipole moment relative to the N–O bond axis, is 1.54. The value of 1.4 ± 0.1 determined from the imaging experiments suggests that dissociation at 308 nm is rapid on the time scale of molecular rotation. A value of -0.5 ± 0.1 for $\beta_0^0(2,2)$ suggests a near limiting alignment of $\mathbf{j}\perp\mathbf{v}$. The bipolar moments measured here are consistent with the prompt dissociation of a cold triatomic molecule, which necessarily yields $\mathbf{j}'$ aligned perpendicular to the molecular plane.

C. Application to bimolecular reactions

The Fourier analysis method has considerable potential for use in ‘‘photoloc’’ experiments on photon-initiated bimolecular reactions. In these experiments velocity-map ion images of the reaction products contain information about the differential cross section and kinetic energy release, as well as angular momentum alignment parameters. In general these cannot be determined by direct inversion of the image, and some form of data fitting is necessary.

The general reaction scheme for a photoloc experiment is

$$AM+h\nu\rightarrow A+M,$$

TABLE III. The even k bipolar moments of the NO product scattering distribution following 308 nm NO_2 photolysis. The moments shown have been renormalized to the more commonly used $\beta_0^K(k_1,k)$ (Ref. 15). Errors in the final digit are given in parentheses. The data obtained in the present experiments are compared with those obtained previously using Doppler-resolved LIF techniques (Ref. 33).

Bipolar moment	Current measurement	Brouard *et al.* (Ref. 33)
$\beta_0^0(0,0)$	1	1
$\beta_0^2(2,0)$	0.70(5)	0.61(2)
$\beta_0^0(2,2)$	−0.50(11)	−0.38(4)
$\beta_0^2(0,2)$	−0.36(2)	−0.23(2)
$\beta_0^2(2,2)$	0.30(7)	0.27(5)
$\beta_0^2(4,2)$	−0.08(6)	−0.27(8)

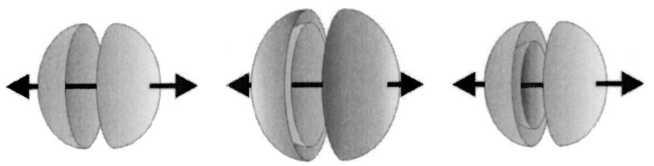

FIG. 9. Imaging applied to reactions: when imaging a photofragment, the radial coordinate provides a measure of the fragment velocity, and the scattering distribution may be well characterized (left); forward-scattered reaction products result in a larger Newton sphere in the lab frame (center); backward scattered products result in a smaller Newton sphere in the lab frame (right).

$$A+BC\rightarrow AB(v',j')+C,$$

In the proposed experiments, a photolysis precursor *AM* and target molecule *BC* (not necessarily a diatomic) are coexpanded in a molecular beam. Polarized laser photolysis of the precursor produces a velocity-aligned photofragment *A* that reacts with the target molecule, and the reaction product $AB(v',j')$ is ionized state-selectively *via* REMPI and detected using velocity-map imaging. In simple photolysis studies, the radial coordinate of a photofragment image simply provides information on the product velocity. However, for a reaction of the kind described previously, the velocity of the center-of-mass of the reacting system will lie approximately along the velocity vector of the fast reactant (i.e., the reactant formed during photolysis of the precursor). When *reaction products* are detected using velocity-map imaging, the radial coordinate of the image is now sensitive to both the product speed distribution and to the angular differential cross section, with "rings" in the images reflecting peaks in either or both of these distributions. This is illustrated schematically in Fig. 9, and discussed in more detail in the following in relation to the current simulations. So long as the scattering distribution of the fast reactant has been well characterized, images of reaction products may be analyzed to return the differential cross section, product speed distribution, and information on product angular momentum polarization. Further details and applications of the photoloc technique may be found in Refs. 17, 34, and 35. An application of the technique in an imaging experiment may be found in the work of Kitsopoulos *et al.* on the $Cl+C_2H_6$ reaction.[36]

As an example, simulated images for the $H+D_2$ reaction, in which the HD product is "detected" *quantum state selectively* (for example, using REMPI techniques), have been fitted using the Fourier moment analysis. The simulations are based on differential cross sections derived from quantum scattering calculations carried out by Aoiz, Bañares, and Castillo[37] at a collision energy of 1.49 eV. The model differential cross sections are used as input to a Monte Carlo simulation of the bipolar moments $b_0^K(k_1,k;v)$ using equations developed in Ref. 17, which are then used to reconstruct the 3D scattering distribution using Eq. (1). Images are obtained by numerical integration of the 3D distribution over the time-of-flight axis. Using this approach, the methods used in generating the simulated images and in performing the analysis are independent, and fitting the simulations provides a stringent test of the performance of the Fourier moment analysis method. Finally, random noise is added to the images to assess the effects that it has on the derived center-of-mass differential cross sections and energy disposals.

As in any three-atom reaction, when the molecular product is detected in a specific quantum state, the total translational energy of the atom plus the detected product (and therefore the velocity of the detected product) has a single well-defined value. In this example, the simulations are carried out at fixed collision energy, with the consequence that the velocity-map images of the HD products are sensitive *only* to the differential cross section of the reaction. The law of cosines relates each scattering angle in the center-of-mass

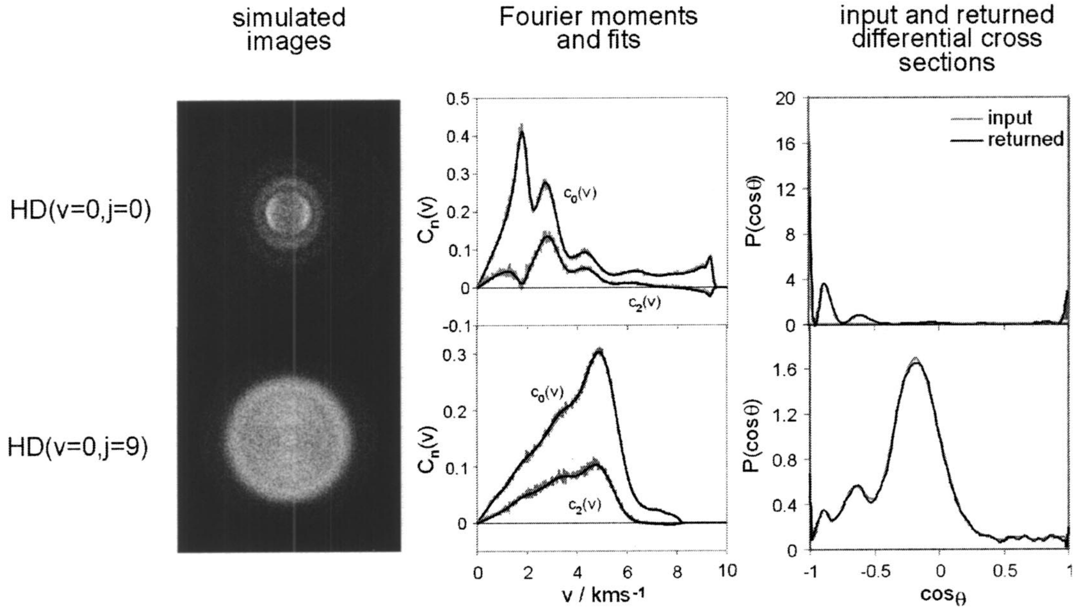

FIG. 10. Simulated images for two HD product quantum states of the $H+D_2$ reaction at a collision energy of 1.49 eV, together with input differential cross sections from quantum scattering theory, and the functions returned from a Fourier moment analysis.

frame to a unique velocity in the lab frame, and in this way, fluctuations in the image intensity along the radial coordinate of the image directly reflect oscillations in the differential cross section.

For comparison two sets of simulations are performed for HD products formed in the $(v=0,j=0)$ and $(v=0, j=9)$ quantum states, chosen for their markedly different differential cross sections, are shown in Figure 10. Also shown in Fig. 10 are the differential cross sections used as input to the simulations and the functions returned from the fitting procedure. The peaks in the differential cross sections are clearly visible as separate rings in the corresponding images. The simulations, and fits to them, demonstrate that using the Fourier moment analysis it is possible to extract even fairly complicated differential cross sections from velocity map images with a high degree of accuracy. The high angular resolution of the method is illustrated by its sensitivity to even the very sharp forward and backward peaks in the $j=0$ differential cross section. The fitting method also appears to be remarkably robust to added noise on the simulated data, with the returned differential cross section faithfully reproducing the input data for even very grainy images.

As discussed previously, for a three-atom reaction the image reflects principally the differential cross section for the chosen product channel of the reaction (in a real experiment, the image will also be affected by the collision energy distribution, particularly if the excitation function varies significantly over the range of collision energies sampled). However, for a reaction in which the coproduct is molecular, the kinetic energy release for the probed channel does not take a single value, and in general the detected product will have a distribution of velocities. It has been shown in a previous paper[34] that the Fourier moment technique is capable of returning both the differential cross section and the kinetic energy release distribution with a high degree of accuracy for a widely varying range of dynamics.

V. CONCLUSION

A new method has been presented for extracting velocity and angular momentum distributions from velocity-map ion images. Based on an analysis of the Fourier moments of a series of images recorded in different experimental geometries, the method is applicable to studies of both photodissociation processes and photon-initiated bimolecular reactions, and suffers from none of the symmetry constraints of the widely used Abel inversion. The technique has been demonstrated by using it to analyze sets of images from two different photolysis processes. For images of the $Cl(^2P_{3/2})$ and $Cl(^2P_{1/2})$ products of 240 nm NOCl photolysis, the Fourier moment analysis methodology returns photofragment speed distributions and anisotropy parameters in good agreement with an inverse Abel transform analysis. When applied to images of state-selected NO fragments from 308 nm photolysis of NO_2, a system for which product rotational alignment is important and the Abel inversion therefore cannot be used, the method returns alignment parameters in good agreement with those determined previously by Doppler-resolved laser-induced fluorescence experiments. The potential of the method for application to bimolecular reactions has been illustrated using simulated images based on the results of recent quantum scattering calculations on the reaction $H+D_2 \rightarrow HD(v=0,j=0,9)+D$. The differential cross sections returned from the analysis procedure are in excellent agreement with those input to the simulations, even when realistic levels of noise are added to the simulated images.

ACKNOWLEDGMENTS

The authors are very grateful to Javier Aoiz, Luis Bañares, and Jesus Castillo for allowing us to use the results of their quantum scattering calculations on $H+D_2$, and to Javier Aoiz and Bruno Martínez-Haya for helpful discussions. We would like to acknowledge Hannah Reisler for providing a preprint of Ref. 14. We would also like to thank the Oxford Supercomputing Center for use of parallel computing facilities, and the EPSRC, the Royal Society and the EU (through Project No. HPRN-CT-1999-00007) for research grants.

[1] C. R. Gehardt, T. P. Rakitzis, P. C. Samartzis, V. Ladopoulos, and T. N. Kitsopoulos, Rev. Sci. Instrum. **72**, 3848 (2001).
[2] T. P. Rakitzis and T. N. Kitsopoulos, J. Chem. Phys. **116**, 9228 (2002).
[3] A. J. R. Heck and D. W. Chandler, Annu. Rev. Phys. Chem. **46**, 335 (1995).
[4] K. R. Castleman, *Digital Image Processing* (Prentice-Hall, Englewood Cliffs, NJ, 1996).
[5] *Imaging in Chemical Dynamics*, edited by A. G. Suits and R. E. Continetti, ACS Symposium Series, Vol. 770 (American Chemical Society, Washington, DC, 2001).
[6] T. P. Rakitzis, Chem. Phys. Lett. **342**, 121 (2001).
[7] B.-Y. Chang, R. C. Hoetzlein, J. A. Mueller, J. D. Geiser, and P. L. Houston, Rev. Sci. Instrum. **69**, 1665 (1998).
[8] M. J. J. Vrakking, Rev. Sci. Instrum. **72**, 4084 (2001).
[9] J. Winterhalter, D. Maier, J. Honerkamp, V. Schyja, and H. Helm, J. Chem. Phys. **110**, 11187 (1999).
[10] K. T. Lorenz, M. S. Westley, and D. W. Chandler, Phys. Chem. Chem. Phys. **2**, 481 (2000).
[11] M. S. Westley, K. T. Lorenz, D. W. Chandler, and P. L. Houston, J. Chem. Phys. **114**, 2669 (2001).
[12] L. S. Bontuyan, A. G. Suits, P. L. Houston, and B. J. Whitaker, J. Phys. Chem. **97**, 6342 (1993).
[13] A. S. Bracker, E. R. Wouters, A. G. Suits, and O. S. Vasyutinski, J. Chem. Phys. **110**, 6749 (1999).
[14] V. Dribinski, A. Ossadtchi, V. Mandelshtam, and H. Reisler, Rev. Sci. Instrum. **73**, 2634 (2002).
[15] R. N. Dixon, J. Chem. Phys. **85**, 1866 (1986).
[16] V. K. Nestorov, R. D. Hinchliffe, R. Uberna, J. I. Cline, K. T. Lorenz, and D. W. Chandler, J. Chem. Phys. **115**, 7881 (2001).
[17] F. J. Aoiz, M. Brouard, and P. Enriquez, J. Chem. Phys. **105**, 4964 (1996).
[18] M. J. Bass, M. Brouard, A. P. Clark, B. Martínez-Haya, and C. Vallance (unpublished).
[19] NIST Atomic Spectra Database, http://physics.nist.gov/cgi-bin/AtData/main_asd
[20] A. C. Kummel, G. O. Sitz, and R. N. Zare, J. Chem. Phys. **88**, 6707 (1987).
[21] A. C. Kummel, G. O. Sitz, and R. N. Zare, J. Chem. Phys. **88**, 7357 (1988).
[22] I. V. Hertel and W. Stoll, Adv. At. Mol. Phys. **13**, 113 (1978).
[23] C. H. Greene and R. N. Zare, Annu. Rev. Phys. Chem. **33**, 119 (1982).
[24] B. M. Haas, P. Felder, and R. Huber, Chem. Phys. Lett. **180**, 293 (1991).
[25] P. Felder and G. P. Morley, Chem. Phys. **185**, 145 (1994).
[26] V. Skorokhodov, Y. Sato, K. Suto, Y. Matsumi, and M. Kawasaki, J. Phys. Chem. A **100**, 12321 (1996).
[27] K. Tonokura, Y. Matsumi, M. Kawasaki, S. Tasaki, and R. Bersohn, J. Chem. Phys. **97**, 8210 (1992).
[28] A. I. Chichinin, Chem. Phys. Lett. **209**, 459 (1993).
[29] M. D. Moser, E. Weitz, and G. C. Schatz, J. Chem. Phys. **78**, 757 (1983).
[30] C. Jonah, J. Chem. Phys. **55**, 1915 (1971).
[31] S. Yang and R. Bersohn, J. Chem. Phys. **61**, 4400 (1974).

[32] G. E. Busch and K. R. Wilson, J. Chem. Phys. **36**, 3638 (1972).
[33] M. Brouard, P. O'Keeffe, D. M. Joseph, and D. Minayev, Phys. Rev. Lett. **86**, 2249 (2001).
[34] M. Brouard, P. O'Keeffe, and C. Vallance, J. Phys. Chem. A **106**, 3629 (2002).
[35] N. E. Shafer-Ray, A. J. Orr-Ewing, and R. N. Zare, J. Phys. Chem. **99**, 7591 (1995).
[36] P. C. Samartzis, D. J. Smith, T. P. Rakitzis, and T. F. Kitsopoulos, Chem. Phys. Lett. **324**, 337 (2000).
[37] L. Bañares (personal communication).